



Constructing Fe/Fe₃C nanocrystals with Fe-N_x sites in Fe-N-C electrocatalyst to achieve high performance for solar cells

Wen Wang^{a,*}, Xueqin Zuo^{a,*}, Qi Yang^b, Qun Yang^a, Huaibao Tang^a, Haijun Zhang^{b,*}, Guang Li^{a,*}

^a School of Materials Science and Engineering, School of Physics and Optoelectronic Engineering, Key Laboratory of Structure and Functional Regulation of Hybrid Materials of Ministry of Education, Anhui Key Laboratory of Information Materials and Devices, Institute of Physical Science and Information Technology, Anhui University, Hefei 230601, China

^b Center for Aircraft Fire and Emergency, Department of Safety Engineering, Civil Aviation University of China, Tianjin 300300, China

ARTICLE INFO

Keywords:

Fe/Fe₃C@NHCF
Electrocatalysis
Counter electrodes
Dye-sensitized solar cells

ABSTRACT

Developing Pt-free counter electrodes (CEs) material for dye-sensitized solar cells (DSSCs) is significant. Herein, we fabricate a catalyst of Fe-N-C by employing N-doped hollow carbon flower (NHCF) as a matrix on which Fe-N_x coordination sites and Fe/Fe₃C nanocrystals (Fe/Fe₃C@NHCF) are mounted and coupled. The DSSC with Fe/Fe₃C@NHCF CE achieves power conversion efficiency (PCE) of 9.37% and highly outperforms the one with Pt CE (7.77%). It is uncovered that Fe/Fe₃C nanocrystals and Fe-N_x coordination sites generate a synergetic effect to enhance catalytic activity of the tri-iodide reduction reaction. The reasons are as follows: (1) Fe/Fe₃C nanocrystals, which possess abundant interfaces and effectively promote the adsorption of reactants on the catalyst surface and charge transfer; (2) Atomically Fe-N_x configurations reduce charge density of Fe atomic centers and quicken reaction kinetics; (3) The unique structure of NHCF matrix almost utilizes all Fe/Fe₃C nanocrystals, providing coupling bridge for nanocrystals with Fe-N_x sites.

1. Introduction

Recently, photovoltaic conversion devices have attracted widespread attention as an advanced technology by which solar energy can be utilized effectively and converted it directly into electricity [1,2]. It is a valuable and effective way of reducing overuse of fossil fuels and developing a global low-carbon economy [3,4]. As the third-generation solar cells, the main technology of dye-sensitized solar cells (DSSCs) is to convert solar radiation into electricity energy via imitating the photosynthesis of plants [5–7]. As far as DSSC is concerned, it is based on the advantages of simple structure, easy manufacturing, and simple production process [8]. Meanwhile, DSSC can also be made into different shapes, various colors and even transparent to meet different requirements in daily life, which have also attracted a lot of attention from researchers [9]. The power conversion efficiency (PCE) of DSSC is mainly determined by the sensitized photoanode, electrolyte and counter electrode (CE). The electrochemical process that directly generates electric current on site is very attractive, in which the oxidation-reduction reaction occurs through the circulation path from I^-

to I_3^- ($3I^- - 2e^- = I_3^-$, $I_3^- + 2e^- = 3I^-$) [10,11]. Among the components of the device, CE is mainly responsible for the collection of electrons in external circuits and the regeneration of the redox couples. At the same time, its electrode material also determines the efficiency and cost of DSSC. Therefore, the research and development of high-performance CE materials is of great significance to DSSC [12,13]. Recently, researchers have made enormous efforts to realize the large-scale business strategy for DSSC and have suggested that the activity of CE materials can significantly enhance the reduction performance for electrolyte-based iodide ions [14–16]. Unfortunately, it is quite difficult to improve PCE in the entire cell, which makes the performance requirements of CE materials even stringent. It is necessary to meet the good conductivity to accelerate electrons transfer, and have outstanding catalytic activity to promote the regeneration of redox couples (I^-/I_3^-). Traditionally, platinum can be acted as CE to meet these necessary requirements. Nevertheless, the low utilization rate and high price of platinum flakes have delayed the development of its commercial applications.

Currently, numerous advanced strategies have been designed to synthesize the non-Pt CE materials, such as forming alloy [17,18],

* Corresponding authors.

E-mail addresses: xqzuo@ahu.edu.cn (X. Zuo), hjzhang_ahu@163.com (H. Zhang), liguang1971@ahu.edu.cn (G. Li).

<https://doi.org/10.1016/j.apcatb.2021.120726>

Received 31 January 2021; Received in revised form 10 September 2021; Accepted 12 September 2021

Available online 16 September 2021

0926-3373/© 2021 Elsevier B.V. All rights reserved.

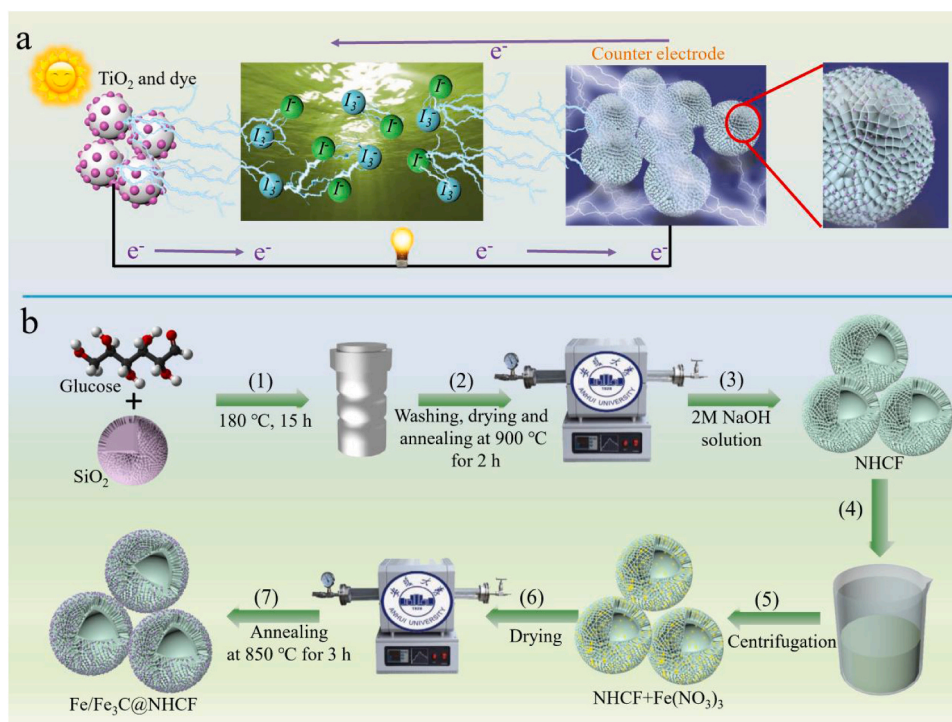


Fig. 1. (a) The working principle diagram of DSSCs, (b) Schematic diagram for the synthesis of $\text{Fe/Fe}_3\text{C@NHCF}$.

interfacial integration etc. [19–22] and these strategies highlight the enriched active sites to improve catalytic activity. For nanocomposite, carbon supports (such as metal-organic framework (MOF) [23], N-doped graphene [24], N-doped carbon nanotube [25], and so on) play an important role in CE performance due to (1) their large specific surface area that can significantly enhance the ability of adsorption for iodide ions; (2) their excellent conductivity that can accelerate electron transfer and effectively restrain coupling of iodide ions; (3) providing support for metal dispersion and maximizing its utilization efficiency. So far, for the metal-nitrogen-carbon (M-N-C) catalysts, there are remain arguments on what are the actual active sites [26–28]. It is generally believed that metal nanoparticles cooperate with catalytically active substances as electron contributors to adjust the adsorption energy of reactants and intermediates. Another common perspective is that the combination of alkali metal ions with nearby active heteroatom sites (N, S, O, etc.) is conducive to stabilizing small metal nanoparticles, reinforcing structural stability and improving catalytic performance. However, there are few reports and investigates on how Fe–N–C catalyst can be acted as CE to alternately catalyze the reduction of tri-iodide in DSSCs. To this end, from the perspective of feasibility and representativeness, we will further insight how atomic-level Fe–N–C integrated with metal nanoparticles can efficiently strengthen the catalytic activity, which would help us understand the active properties of Fe–N–C materials.

Herein, we first used the template method to prepare NHCF as a substrate. Subsequently, a high-active Fe–N–C catalyst was synthesized by high temperature pyrolysis, and then $\text{Fe/Fe}_3\text{C}$ nanoparticles and Fe–Nx coordination sites (denoted as $\text{Fe/Fe}_3\text{C@NHCF}$) were constructed on NHCF. As a result, the $\text{Fe/Fe}_3\text{C}$ nanocrystals are formed by aggregated iron atoms. Simultaneously, the pyrolysis process can produce the Fe–Nx configurations sites around $\text{Fe/Fe}_3\text{C}$ nanoparticle. Electrochemical test and photocurrent density voltage (J - V) test indicate that DSSC assembled with the $\text{Fe/Fe}_3\text{C@NHCF}$ composite containing $\text{Fe/Fe}_3\text{C}$ interface and Fe–Nx sites exhibits superior reaction kinetics and an excellent PCE of 9.37%, which is much higher than commercial Pt (7.77%), $\text{Fe/Fe}_3\text{C@HCF}$ (7.89%) and HCF (3.81%). It suggests that $\text{Fe/Fe}_3\text{C}$ nanocrystals and Fe–Nx play pivotal parts in whole catalysts. Additionally, X-

ray photoelectron spectroscopy (XPS) combined with the first-principle calculation further reveals that $\text{Fe/Fe}_3\text{C@NHCF}$ can not only reduce the charge density on central Fe atom to optimize its catalytic activity, but also enhance atomic iodine adsorption ability on the $\text{Fe/Fe}_3\text{C}$ interface region. Therefore, the high catalytic activity of this material mainly originates from the synergistic effect of $\text{Fe/Fe}_3\text{C}$ nanoparticles and Fe–Nx configurations sites. This work uncovers the principal cause of the great catalytic activity of the Fe–N–C catalysts and provides a resolution for developing greatly active electrode materials in DSSCs.

2. Experimental section

2.1. Synthesis of SiO_2 sphere flower

Typically, 0.2 g urea and 0.2 g cetylpyridine bromide were dissolved in 15 mL deionized water under magnetic stirring to form a homogeneous solution, which is labeled as solution A. Then, 2 mL tetraethyl orthosilicate, 0.2 mL n-amyl alcohol and 20 mL cyclohexane were mixed and stirred, which is labeled as solution B. Subsequently, solution A and solution B were well mixed, and transferred into a Teflon-lined autoclave for reaction at 100°C for 12 h. The production was centrifugally collected after multiple cleaning, and finally heated at 550°C for 5 h.

2.2. Synthesis of HCF and NHCF

0.1 g SiO_2 was added to 30 mL methylbenzene, then 0.1 mL 3-aminopropyltrimethoxysilane was poured in this mixed solution and kept at 65°C for 12 h. The resulting suspension was centrifuged and washed three times using deionized water and dried. The obtained samples were poured into glucose solution and then transferred into a Teflon-lined autoclave and maintained at 180°C for reaction for 12 h. The samples were centrifuged and dried. Finally, the sample was annealed at 900°C for 2 h to obtain HCF. To get NHCF, the sample and tripolycyanamide were mixed evenly, and then also annealed at 900°C for 2 h.

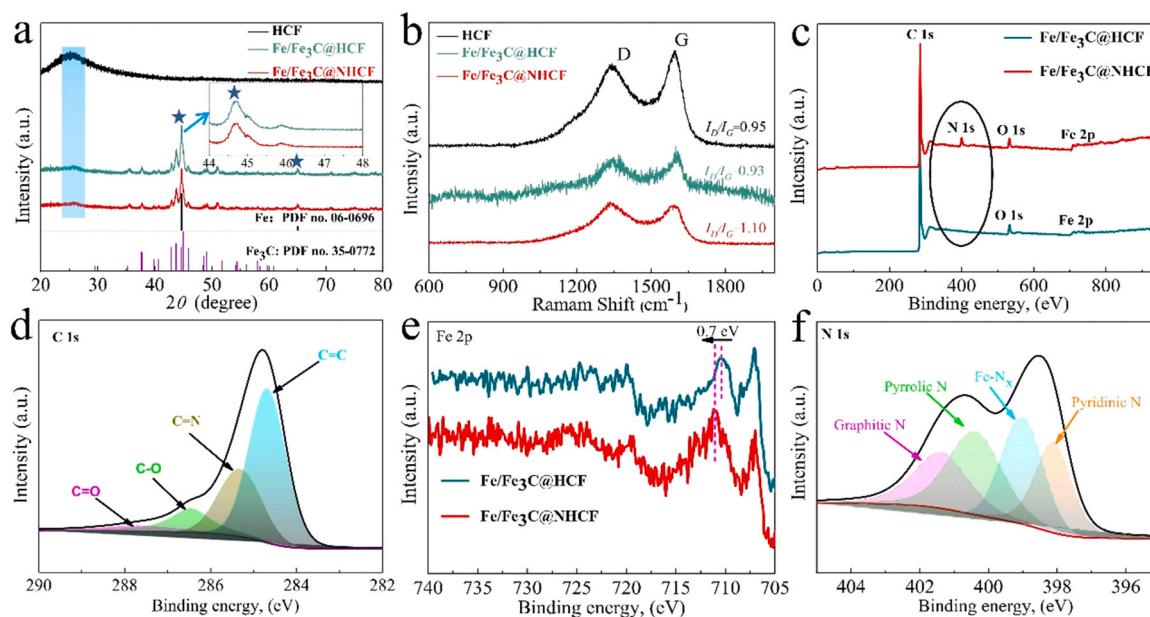


Fig. 2. (a) XRD patterns of HCF, Fe/Fe₃C@HCF, Fe/Fe₃C@NHCF, (b) the Raman spectrum of HCF, Fe/Fe₃C@HCF, Fe/Fe₃C@NHCF, (c) The wide XPS spectra of Fe/Fe₃C@HCF, Fe/Fe₃C@NHCF, (d) C 1s spectra, (e) Fe 2p spectra, (f) N 1s spectra.

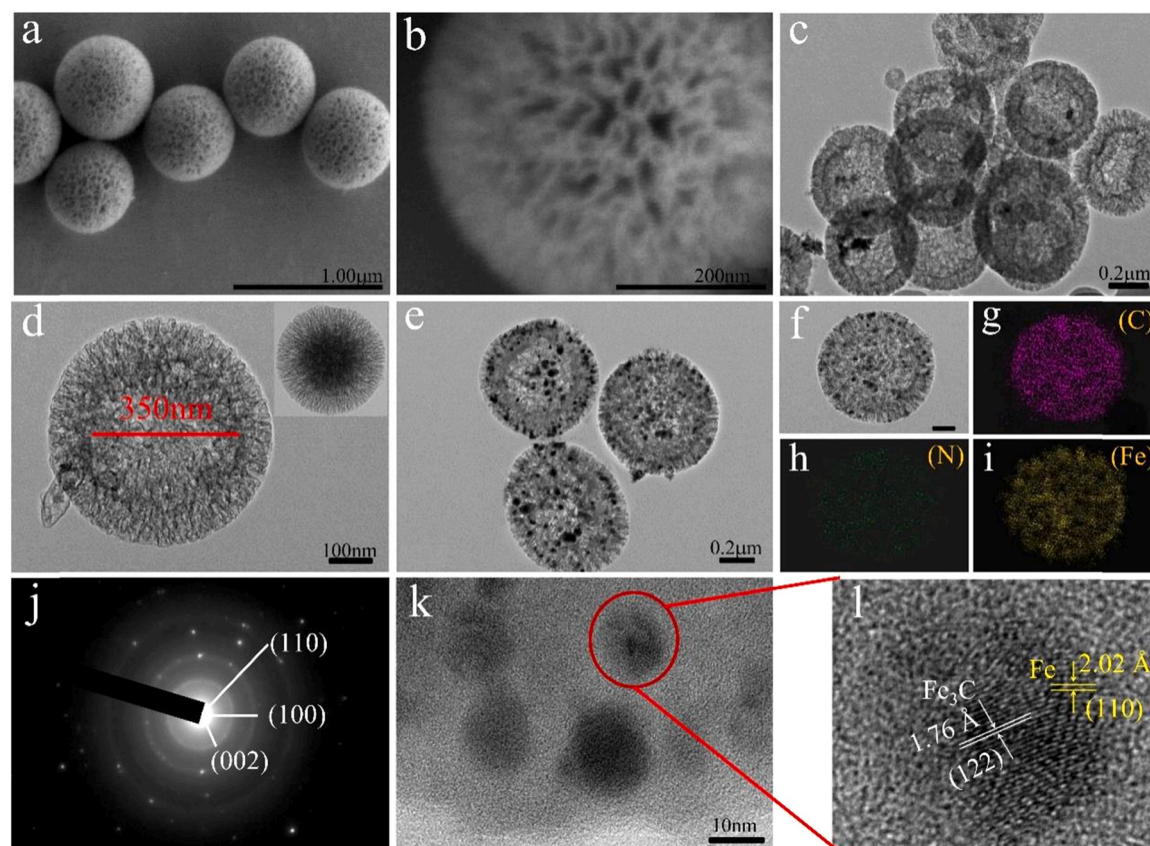


Fig. 3. (a and b) SEM images of SiO₂ spherical flowers, (c and d) TEM images of NHCF, the inset of Figure d: TEM image of SiO₂, (e) TEM image of Fe/Fe₃C@NHCF. (f-i) The corresponding elemental mapping images of (g) C element, (h) N element, (i) Fe element. (j) The SAED image for Fe/Fe₃C@NHCF, (k) The HRTEM image of Fe/Fe₃C@NHCF. (l) The lattice fringes of material.

2.3. Synthesis of Fe@HCF, Fe₃C@HCF and Fe/Fe₃C@HCF composite

Typically, 0.2 g HCF was poured into Fe(NO₃)₃ solution and constantly stirred for 24 h. Subsequently, the sample was centrifuged

and dried, and then annealed at 600 °C for 2 h to form Fe@HCF, at 850 °C for 3 h to form Fe/Fe₃C@HCF, and at 850 °C for 5 h to obtain Fe₃C@HCF, respectively.

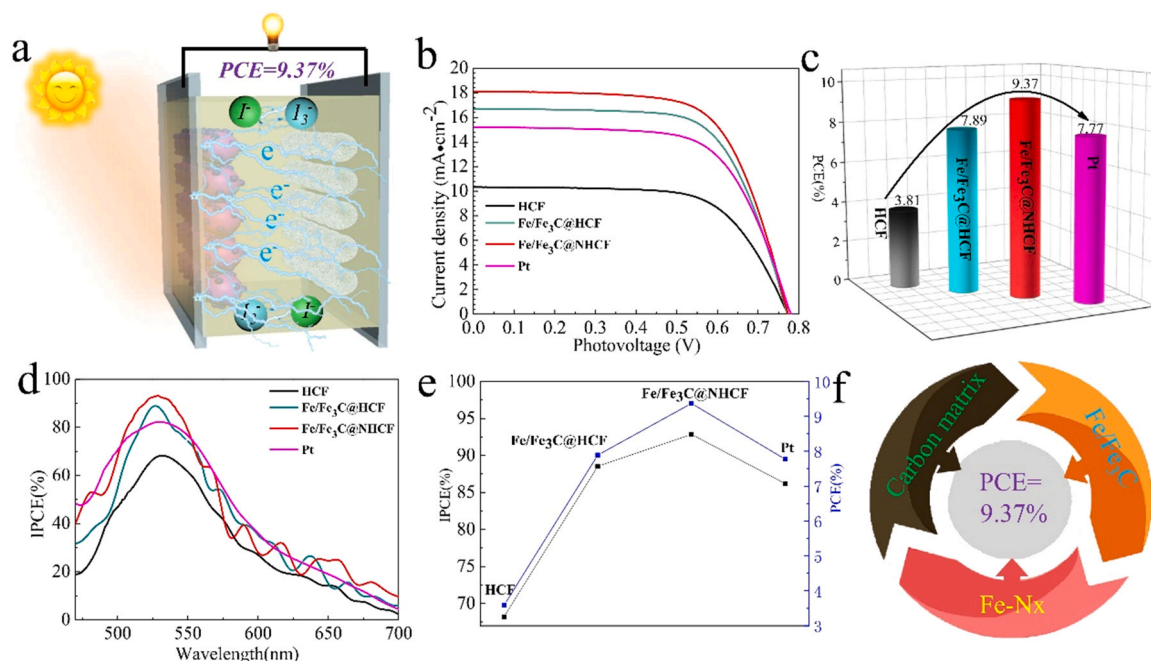


Fig. 4. (a) Schematic structure of a DSSC using Fe/Fe₃C@NHCF as the CE to form a full cell, (b) *J*–*V* curves of DSSCs with different CEs, (c) PCE for all samples including a DSSC with the CE made of Pt, (d) IPCE curves of DSSCs with different CEs, (e) An associated diagram between PCE and IPCE, (f) carbon matrix, Fe/Fe₃C heterostructure and Fe-Nx sites synergistically obtain high conversion efficiency.

Table 1

Photovoltaic parameters for DSSCs based on testing of different CEs in the same environment (*J*_{SC}, *V*_{OC} and *FF* represent the short-current densities, open-circuit voltages and fill factors, respectively.).

CEs	<i>J</i> _{SC} (mA·cm ⁻²)	<i>V</i> _{OC} (V)	<i>FF</i> (%)	PCE (%)
HCF	10.33	0.775	47.59	3.81
Fe/Fe ₃ C@HCF	16.71	0.765	61.72	7.89
Fe/Fe ₃ C@NHCF	18.11	0.775	66.76	9.37
Pt	15.21	0.785	66.08	7.77

2.4. Synthesis of Fe/Fe₃C@NHCF composite

0.2 g HCF was poured into Fe(NO₃)₃ solution and constantly stirred for 24 h. Subsequently, the sample was centrifuged and dried. The obtained sample and tripolycyanamide were mixed evenly, and annealed at 850 °C for 3 h to form Fe/Fe₃C@NHCF.

Fabrication of CE, assembly of DSSC, computational details, part of the characterization and measurements are displayed in [Supporting Information](#).

Table 2

In recent years, the photoelectric conversion efficiency and parameters of DSSCs constructed with CEs of different materials.

CEs	<i>J</i> _{SC} (mA·cm ⁻²)	<i>V</i> _{OC} (V)	<i>FF</i> (%)	PCE (%)	Ref.
Fe/Fe ₃ C@NHCF	18.11	0.775	66.76	9.37	This work
Ti ₁ /rGO	16.53	0.840	64.00	8.83	Adv. Mater. 2020 , 2000478 DOI: 10.1002/adma.202000478
CuFeS ₂	17.32	0.665	73.34	8.10	Chem. Commun. 2016 , 52(77), 11488–11491. DOI: 10.1039/C6CC06241E
GCT-F	16.64	0.790	68.00	8.94	Chem. Mater. 2017 , 29(22), 9680–9694. DOI: 10.1021/acs.chemmater.7b03385
ZIF-ZnSe-NC-11 wt%	16.40	0.770	69.00	8.69	J. Mater. Chem. A 2018 , 6 (12), 5107 DOI: 10.1039/C8TA00968F
CoFeNiMo@NCNT-800–8–5	14.71	0.731	60.00	6.46	Appl. Catal. B: Environ. 280 2021 , 119421 DOI: 10.1016/j.apcatb.2020.119421

3. Results and discussion

The working conditions of DSSC and its key components are clearly defined in [Fig. 1a](#), and it can be clearly seen that CE mainly acts as the role of electron transfer. At the same time, the interface between CE and electrolyte can effectively catalyze the redox regeneration of iodide ions. Therefore, the necessary condition for obtaining high PCE is that the CE must meet high conductivity and excellent catalytic activity of iodide ion. [Fig. 1b](#) reflects the synthesis process of Fe/Fe₃C@NHCF.

3.1. Structural Information

First, in order to examine the nature of the crystal structure of the given materials, X-ray diffraction (XRD) was used to record their corresponding patterns, as shown in [Fig. 2a](#). The XRD patterns of HCF, Fe/Fe₃C@HCF and Fe/Fe₃C@NHCF demonstrated an obvious peak at 26.1°, which could be distributed to graphitic carbon. As shown in [Fig. S1a](#), we can clearly find the absence of iron phase, suggesting Fe atoms can be combined with the carbon matrix through a disorderly dispersal in HCF/Fe(NO₃)₃. After 650 °C annealed with tripolycyanamide, two peaks were situated at 44.6° and 65.0°, which were well indexed to the (110) and (200) planes of Fe ([Fig. S1b](#)) (JCPDS no. 06–0696) [23]. As the temperature increased to 850 °C, besides two

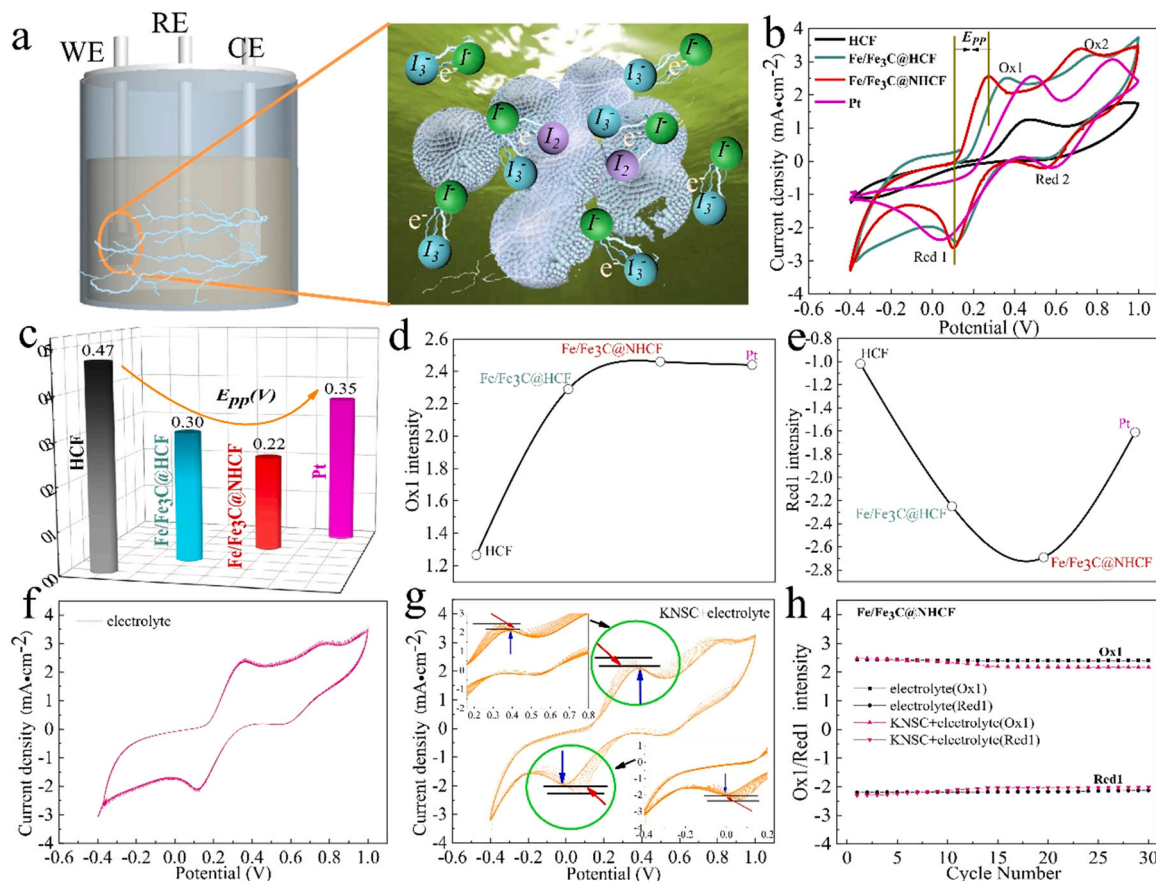


Fig. 5. (a) Schematic diagram of I^-/I_3^- in Fe/Fe₃C@NHCF adsorption, dissociation and desorption during CV measurement (WE: Working electrode, RE: Reference electrode, CE: Counter electrode), (b) Cyclic voltammograms of the Pt and all as-prepared samples nanostructures for the redox of I^-/I_3^- species, (c) The E_{pp} of all samples and Pt, (d) Ox1 intensity, (e) Red1 intensity, (f) the stability of Fe/Fe₃C@NHCF in electrolyte, (g) the stability of Fe/Fe₃C@NHCF in electrolyte containing SCN⁻, (h) Ox1/Red1 intensity of Fe/Fe₃C@NHCF in different electrolyte system.

Table 3

The calculated adsorption energies (E_{ad} in eV) of iodine atom on Fe/Fe₃C@HCF and Fe/Fe₃C@NHCF.

Adsorption Site	Fe/Fe ₃ C@HCF	Nitrogenated Fe/Fe ₃ C@NHCF
Fe cluster	-2.62	1.78
Fe ₃ C cluster	-5.25	-3.85
Fe-Fe ₃ C Interface	-6.68	3.41

peaks of 44.6° and 65.0°, the extra peaks in line well with that of Fe₃C species appeared (JCPDS no. 35-0722) [29]. It shows that Fe species are amassed into the Fe/Fe₃C mixed phase at high temperature.

The graphitization degree and defects of the pure HCF, Fe/Fe₃C@HCF and Fe/Fe₃C@NHCF were further performed via the Raman spectra (Fig. 2b). Remarkably, the D and G bands were located in 1352 cm⁻¹ and 1580 cm⁻¹ indicated the messy graphitic carbon and the E_{2g} vibration of the sp²-bonded carbon atoms [22,30]. Additionally, the higher I_D/I_G value of the Fe/Fe₃C@NHCF was obtained by comparison with that of Fe/Fe₃C@HCF, revealed the coexistence of more defects. This means that nitrogen atoms have been successfully introduced and improves the electrical conductivity of carbon material and expedites the charge transfer.

The chemical composition and binding state of the Fe/Fe₃C@HCF and Fe/Fe₃C@NHCF were further investigated via XPS full spectrum, as shown in Fig. 2c. Noteworthy, N elements clearly emerge in Fe/Fe₃C@NHCF compared with Fe/Fe₃C@HCF. For Fe/Fe₃C@NHCF, in the C1s region (Fig. 2d), the peak at 285.34 eV can be attributed to C-N, implying the doping of nitrogen in the carbon substrate [7]. The

high-resolution spectrum of Fe 2p (Fig. 2e) was located at 706.92 eV and 708.41 eV, and could be well assigned as zero-valence Fe (metallic iron or carbide) and Fe²⁺. Moreover, the peaks of Fe/Fe₃C@NHCF observed near around 710 eV could be safely attributed to Fe in Fe-Nx configuration [31]. Interestingly, the Fe peak of Fe-Nx configuration tends to partially positive shifts (710.36–711.03 eV) compared with Fe/Fe₃C@HCF. This shift indicates the electronic interaction between Fe and N leads to a decrease in the charge density of the central Fe atoms. This is a quite valuable evidence for the interaction of Fe-Nx and Fe-C [32]. Fig. 2f displays the high-resolution N1s spectrum of the Fe/Fe₃C@NHCF, which can be divided into 4 peaks: pyridinic N (398.17 eV), Fe-Nx (399.04 eV), pyrrolic N (400.42 eV), and graphitic N (401.41 eV) [33]. It is worth noting that the peaks of Fe-Nx species also signifies the interaction of atomic-level Fe and N-doped carbon matrix and those species are extensively known as crucial groups for catalytic reactions.

3.2. Morphological analysis

It can directly reflect the morphological evolution of NHCF to Fe/Fe₃C@NHCF through scanning electron microscope (SEM) and transmission electron microscopy (TEM). SEM image (Fig. 3a) displays multiple nanospheres that possess uniform size (about 450 nm in diameter). Moreover, a mass of thin nanosheets were regularly self-assemble to form hollow carbon flower, which can be clearly found in Fig. 3b. The internal structure of NHCF is investigated through TEM images (Fig. 3c and d) under different magnification. Interestingly, we find that the NHCF is hierarchical hollow structure with a much larger

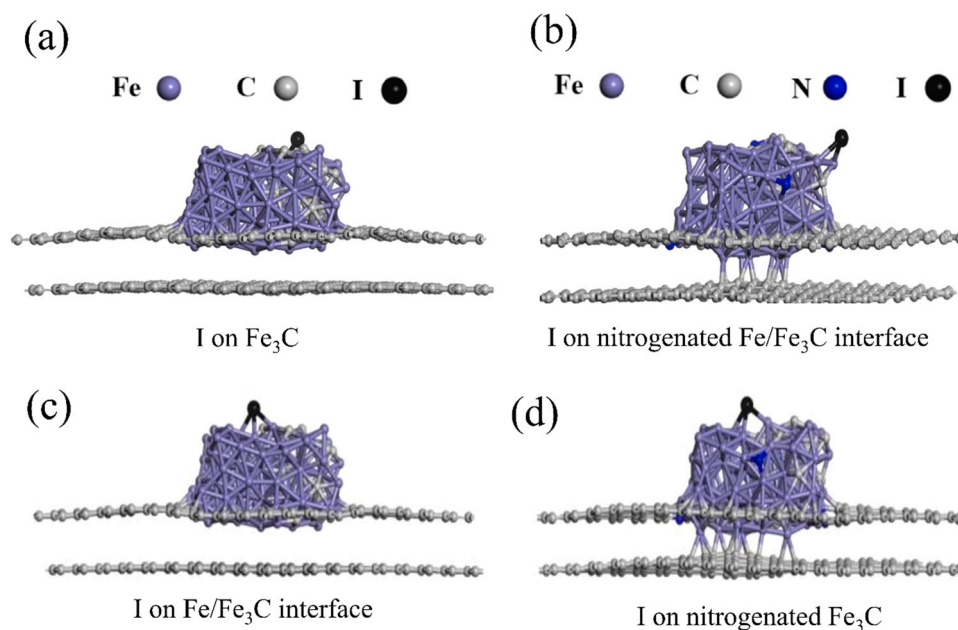


Fig. 6. (a) and (c) Geometric structures of iodine atom adsorbed on Fe/Fe₃C@HCF, (b) and (d) Geometric structures of iodine atom adsorbed on nitrogenated Fe/Fe₃C@NHCF.

degree of internal hollowness (350 nm), benefiting from the removal of the pure hierarchical SiO₂ spheres. The morphology of SiO₂ spheres is inserted in Fig. 3d and Fig. S2a, S2b. The obtained structure can effectively avoid ‘dead volume’ and strengthen the full contact with the electrolyte. As shown in Fig. 3e, the fine Fe/Fe₃C nanoparticles are evenly anchored on the surface of NHCF, which is helpful to maximize the utilization efficiency of Fe/Fe₃C nanoparticles. In addition, the distribution of chemical elements for Fe/Fe₃C@NHCF was verified by an elemental mapping. Fig. 3f-i clearly shows that the components of Fe, C and N are uniformly dispersed in the given materials. Notably, the several rings and scattered dots are displayed in the corresponding SAED pattern (Fig. 3j), which could be allocated to diffraction planes of the graphitic carbon shell and crystalline Fe₃C. The high-resolution transmission electron microscopy (HRTEM) image of the Fe/Fe₃C@NHCF (Fig. 3k) displays multiple nanoparticles and those nanoparticles are near around 10 nm in diameter. Among them, zoom in red areas (Fig. 3l), the different lattice fringes with a spacing of 0.176 nm and 0.202 nm, which matches well with the (122) plane of Fe₃C and the (110) plane of Fe. N₂ adsorption and desorption analyses are exposed in Fig. S3, and prove that the surface area of Fe/Fe₃C@NHCF is 282 cm³ g⁻¹. It can contribute to the adsorption of iodide ions and speed up the reaction kinetics.

3.3. Electrochemical analysis

The working state of the full cell is simulated in Fig. 4a. In the whole process, the working principle of DSSCs is analogous to that of photosynthesis. The dye molecules are excited via absorbing light to generate electrons and then the electrons are transferred from photoanode to CE [34]. Moreover, the high reduction activity of CE to tri-iodide can efficiently hinder the electrons and holes recombination at the photoanode. Therefore, the outstanding catalytic activity and conductivity of CE materials are necessary conditions for high PCE. The photocurrent density-voltage (*J*-*V*) curves (Fig. 4b) were implemented to evaluate the PCE under the simulated illumination (AM 1.5, 100 mW·cm⁻²) [35–37]. We conducted several tests on the results of the given samples, and the final result is the average of the multiple test data, as shown in Fig. S4. The PCE value of samples from high to low is Fe/Fe₃C@NHCF (9.37%), Fe/Fe₃C@HCF (7.89%), Pt (7.77%), HCF (3.81%), as shown in Fig. 4c.

The related photovoltaic parameters with fill factor (FF), short-circuit current density (*J*_{sc}), open circuit voltage (*V*_{oc}), and PCE are listed in Table 1. In recent years, DSSCs constructed with different CE materials achieve the value of PCE and related parameters are displayed in Table 2. It is noteworthy that DSSC with Fe/Fe₃C@NHCF CE obtained the highest PCE, which outperformed that of using the other given CEs and even far greater than Pt-based CE device. It can be inferred that Fe/Fe₃C@NHCF possess prominent regenerative ability for I⁻. Obviously, the present work suggests that the NHCF conductive nanoreactor integrated with the interface Fe/Fe₃C and Fe-N_x configurations sites may be the main reason for high catalytic performance.

Based on the above results, the incident photon to current conversion efficiency (IPCE) spectra (wavelength ranging from 450 nm to 700 nm) with all given materials are obtained and clearly shown in Fig. 4d. This is another very significant characteristic test to detect the performance of DSSC, which represents the photon-to-electron conversion efficiency. The IPCE value of Fe/Fe₃C@NHCF is significantly higher than the value based on other CE materials. The corresponding order of IPCE value is Fe/Fe₃C@NHCF (92.86%) > Fe/Fe₃C@HCF (88.53%) > Pt (86.16%) > HCF (68.2%). The short-circuit photocurrent is obtained by evaluating the IPCE result of given materials, which integrate the action spectra in the 430–720 nm range [38]. Results of these calculations are 10.73 mA cm⁻² (HCF), 17.06 mA cm⁻² (Fe/Fe₃C@HCF), 18.63 mA cm⁻² (Fe/Fe₃C@NHCF) and 15.82 mA cm⁻² (Pt), and the integrated current see Fig. S5. Offering forceful evidence that the Fe/Fe₃C@NHCF is excellent CE material for DSSCs.

To further support the above conclusion, the cyclic voltammetry (CV) curves were implemented to directly assess the catalytic performance for the tri-iodide activity of those materials [39,40]. The adsorption and desorption behavior of iodide ions in CE surface is displayed in Fig. 5a and the CV curve (Fig. 5b) emerges two pairs of peaks (marked as Red1/Ox1 and Red2/Ox2) [41–43]. The Red1/Ox1 corresponds to lower potential, allocating to Eq. (1). Meanwhile, the Red2/Ox2 corresponds to higher potential, attributed to Eq. (2).



In practice, the real value of Red1/Ox1 is significantly higher than

theoretical value for catalytic performance of CE materials. Typically, there are two important parameters which are peak current density and peak-to-peak gap (termed as E_{pp}) [44–46], reflecting reversibility and reaction rate, respectively. The E_{pp} values order (from high to low) of all prepared materials is HCF, Pt, Fe/Fe₃C@HCF, and Fe/Fe₃C@NHCF, which is presented in Fig. 5c. Fe/Fe₃C@NHCF showed the ability of rapid reduction of iodide ($I^- \leftrightarrow I_3^-$) and the reduction rate of iodide accelerated the regeneration of dye molecules [47]. Furthermore, seen from simple curve graphs in Fig. 5d and e (peak current density of Red1 and Ox1), the Ox1 value of Fe/Fe₃C@NHCF is 2.46 mA cm⁻², which is higher than that of pure Pt CE (2.44 mA cm⁻²) and other given CE materials. The Red1 value of Fe/Fe₃C@NHCF is -2.69 mA cm⁻², which is lower than that of pure Pt CE (-1.61 mA cm⁻²) and other given CE materials. It indicates that the reduction activity of Fe/Fe₃C@NHCF is excellent to triiodide compared with other given materials. Moreover, the Tafel curves and electrochemical impedance spectroscopy (EIS) measurement (Fig. S6 and S8) are also performed by constructing a function between the current and applied potential to further identify catalytic kinetics of CE materials. We conducted several tests on the results of the given samples, and the final result is the average of the multiple tests data, as shown in Fig. S7, S9. In the Fig. S10, the *J-V* properties of 5 DSSCs assembled by the Fe/Fe₃C@NHCF were tested. It was found that the *J-V* properties (including J_{SC} , V_{OC} , FF and PCE) of the Fe/Fe₃C@NHCF fluctuate in a certain range, but the PCE values were all higher than 9, indicating that the Fe/Fe₃C@NHCF possess good photovoltaic properties and the corresponding sections are detailed in the Supporting Information. Additionally, in Fig. S11a, cyclic voltammetry curves of Fe/Fe₃C@NHCF CE at the changed scanning speeds (10, 30, 50, 70, 90 mV s⁻¹) are displayed. The relationship between cathodic and anodic peak current densities is a linear relationship (Fig. S11b), which suggests a stable reaction process. The high performance may be ascribed to Fe/Fe₃C nanocrystals coupling with Fe-Nx coordination sites evenly distributed on the carbon matrix with high specific surface area. To identify the role of Fe/Fe₃C interfaces, Fe@HCF, Fe₃C@HCF and Fe/Fe₃C@HCF components were also successfully synthesized as the control samples to further identify the effect of abundant interfaces on iodide ions adsorption via *J-V* and CV curve analysis (Fig. S12). The related CV and *J-V* curves analysis of HCF and NHCF were presented in Fig. S13. It is revealed that E_{pp} , the Ox1 intensity and Red1 intensity of Fe/Fe₃C@HCF is far better than the pure Fe@HCF and Fe₃C@HCF, suggesting the abundant interfaces are not only beneficial to adsorb more I^- and I_3^- , but also speeding up electron transfer [48]. Additionally, the value of E_{pp} and Ox1 intensity and Red1 intensity for Fe/Fe₃C@NHCF is superior to the value of Fe/Fe₃C@HCF, attributing to the introduction of Fe-Nx configurations sites integrated with Fe/Fe₃C nanocrystals the further improvement of the catalytic activity.

As we all know, the thiocyanate (SCN⁻) ion can damage Fe-Nx sites in oxygen reduction reaction [49,50]. Considering whether the reaction between SCN ions and iodine electrolyte will greatly affect the CV reaction parameters, we firstly measured the Pt activity and found that the change of E_{pp} is almost negligible (Fig. S14). However, the E_{pp} , Ox1 and Red1 intensity of CV curve significantly decay for Fe/Fe₃C@NHCF nanocomposite when electrolyte contains Potassium Thiocyanate (KSCN), which is presented in Fig. 5f, g. Fig. 5h clearly shows the changes of Ox1 and Red1 peak intensity for Fe/Fe₃C@NHCF electrode material, which indicate that the significant reduction of catalytic activity can be ascribed to the obstructive of Fe-Nx sites by SCN⁻ in catalyzing. This speculation indicates that the Fe-Nx site may have a great influence on the tri-iodide catalytic performance of Fe/Fe₃C@NHCF. In order to further test the photoelectric performance of the given material after a long period of work, we conducted a 168 h *J-V* curve test, as shown in the Fig. S15. The results show that the final PCE value of Fe/Fe₃C@NHCF is 7.45, which is 79.5% of the original value (9.37%). But at the time, the PCE value of Pt was 4.78, which is only 61.5% of the origin alone (7.77%). Therefore, the stability performance of DSCs vs. time of Fe/Fe₃C@NHCF as the CE in the DSSC is much better than the

one with standard Pt as CE. All above the results show that DSSC with Fe/Fe₃C@NHCF CE has good long-term stability and photoelectric properties, which exceeds that of Pt CE.

The combined calculations also reveal that all the adsorption energy (E_{ad}) of iodine atom on Fe/Fe₃C@HCF is negative, indicating the relative difficulty of iodine adsorption on Fe/Fe₃C@HCF before nitrogenation. For the nitrogenated Fe/Fe₃C@HCF, the iodine adsorption on the Fe/Fe₃C interface region is the most preferable in energy, which implies the excellent capability of nitrogenated Fe/Fe₃C@HCF for capturing iodine atom. Suggested by the generally more positive E_{ad} of iodine atom on nitrogenated Fe/Fe₃C@HCF than that of the untreated Fe/Fe₃C@NHCF, the nitrogenation of Fe/Fe₃C@NHCF should result in the higher efficiency of electron transfer between the CE and electrolyte. The related E_{ad} of given materials are listed in Table 3.

Additionally, the M ulliken populations were also analyzed to investigate the electron distribution of the highest- E_{ad} systems for Fe/Fe₃C@HCF sheets with and without nitrogen, which are models represented in Fig. (6a-d) and Fig. S16, respectively. It was found that the electron population of adsorbed iodine atoms on the untreated and nitrogenated Fe/Fe₃C@HCF sheets are 0.07 e and 0.26 e, respectively, indicating the abundance of electrons on the iodine atom adsorbed on the nitrogenized material. Therefore, the nitrogenation of Fe/Fe₃C@NHCF should lead to higher efficiently transferred electrons than that of untreated Fe/Fe₃C@HCF. Moreover, isosurfaces of electron location function plotted (Fig. S17) with the value of 0.7 au for iodine adsorbed on Fe/Fe₃C@HCF and Fe/Fe₃C@NHCF. Given all this, the interface synergy between Fe/Fe₃C and Fe-Nx configurations sites is the main source of high performance in DSSCs.

4. Conclusions

Taking advantage of interface synergy between Fe/Fe₃C and atomic-level Fe-Nx sites, we have developed iron source and nitrogen co-implanted inside a hollow carbon flower matrix as a novel CE to tri-iodide catalysis. The analysis results prove that the Fe/Fe₃C nanoparticles and Fe-Nx configuration co-exist in the catalyst. We discovered that pyrolysis is important for Fe-based catalysts, this constructs the Fe-N_x configuration at the atomic level. Additionally, carbon also restricts the Fe/Fe₃C nanocrystals agglomeration to form rich interface structure with enlarged active surfaces, which offers robust chemical affinity for tri-iodide. Meanwhile, first-principle calculations also unambiguously come to the conclusion that Fe/Fe₃C nanocrystals of the neighboring Fe-Nx can significantly inhibit tri-iodide coupling and promotes tri-iodide catalyzation with fast redox kinetics. These electrode materials with featuring superiorities endow outstanding performance and cyclability even at long working conditions. We think that Fe-N-C catalyst materials for DSSCs will stimulate more efforts to exploit great potential with combining interface engineering with local electronic structure optimization. The unique engineered 3D conductive substrate strategy also offers ideas for rational structural design in energy conversion and storage systems.

CRediT authorship contribution statement

Wen Wang: Conceptualization, Methodology, Software, Writing – original draft, preparation, Writing – review & editing. **Xueqin Zuo:** Data curation. **Qi Yang:** Visualization, Investigation. Qun Yang, Huai-bao Tang, Haijun Zhang, Writing – review & editing. **Guang Li:** Resources, Writing – review & editing, Conceptualization, Methodology, Project administration, Supervision, Validation.

Declaration of Competing Interest

The authors declare that they have no known competing financial interests or personal relationships that could have appeared to influence the work reported in this paper.

Acknowledgments

This work was financially supported by National Key R&D Program of China (2017YFA0403503), National Natural Science Foundation of China (11674001), Open fund for Discipline Construction, Institute of Physical Science and Information Technology (S01003103, Anhui University), The Recruitment Program for Leading Talent Team of Anhui Province (LTIT20200002), the Key Projects of Natural Science Research in Universities of Anhui Province (KJ2020A0018), the Key Natural Science Research Program of Anhui Educational Committee (KJ2018ZD001), and the Doctoral Research Start-up Funds projects of Anhui University (J01003201), Thank you for XFANO Materials Tech Co. Ltd. (Nanjing, China).

Appendix A. Supporting information

Supplementary data associated with this article can be found in the online version at [doi:10.1016/j.apcatb.2021.120726](https://doi.org/10.1016/j.apcatb.2021.120726).

References

- [1] D.H. Kwon, J.B. Baek, Edge-functionalized graphene nanoplatelets as metal-free electrocatalysts for dye-sensitized solar cells (Article), *Adv. Mater.* 31 (2019), 1804440, <https://doi.org/10.1002/adma.201804440>.
- [2] L. Meng, J. You, Y. Yang, Addressing the stability issue of perovskite solar cells for commercial applications (Article), *Nat. Commun.* 9 (2018), 5265, <https://doi.org/10.1038/s41467-018-07255-1>.
- [3] S.P. Borderud, Y. Burkhalter, J. Song, Y. Liu, S. Liang, Z. Liu, C. Hao, J. Qiu, Erratum: SP, Li Y, Burkhalter JE, CE and Ostroff JS. Electronic cigarette use among patients with cancer: Characteristics of electronic cigarette users and their smoking cessation outcomes (Article), *Cancer* 121 (2015), 800, <https://doi.org/10.1002/aenm.201500180>.
- [4] H. Liu, X. Qian, Y. Niu, M. Chen, C. Xu, K.-Y. Wong, Hierarchical Ni-MoSe₂@CoSe₂ core-shell nanosphere as highly active bifunctional catalyst for efficient dye-sensitized solar cell and alkaline hydrogen evolution (Article), *Chem. Eng. J.* 383 (2020), 123129, <https://doi.org/10.1016/j.cej.2019.123129>.
- [5] M. Zhao, K. Yuan, Y. Wang, G. Li, J. Guo, L. Gu, W. Hu, H. Zhao, Z. Tang, Metal-organic frameworks as selectivity regulators for hydrogenation reactions, *Nature* 539 (2016) 76–80, <https://doi.org/10.1038/nature19763>.
- [6] L. Zhang, X. Yang, W. Wang, G.G. Gurzadyan, J. Li, X. Li, J. An, Z. Yu, H. Wang, B. Cai, A. Hagfeldt, L. Sun, 13.6% Efficient organic dye-sensitized solar cells by minimizing energy losses of the excited state, *ACS Energy Lett.* 4 (2019) 943–951, <https://doi.org/10.1021/acsenrgylett.9b00141>.
- [7] X. Meng, C. Yu, X. Zhang, L. Huang, M. Rager, J. Hong, J. Qiu, Z. Lin, Active sites-enriched carbon matrix enables efficient triiodide reduction in dye-sensitized solar cells: an understanding of the active centers, *Nano Energy* 54 (2018) 138–147, <https://doi.org/10.1016/j.nanoen.2018.09.070>.
- [8] W. Yang, Z. Li, X. Xu, L. Hou, Y. Tang, B. Deng, F. Yang, Y. Wang, Y. Li, Atomic N-coordinated cobalt sites within nanomesh graphene as highly efficient electrocatalysts for triiodide reduction in dye-sensitized solar cells, *Chem. Eng. J.* 349 (2018) 782–790, <https://doi.org/10.1016/j.cej.2018.05.139>.
- [9] H. Michaels, M. Rinderle, R. Freitag, I. Benesperi, T. Edvinsson, R. Socher, A. Gagliardi, M. Freitag, Dye-sensitized solar cells under ambient light powering machine learning: towards autonomous smart sensors for the internet of things, *Chem. Sci.* 11 (11) (2020) 2895–2906.
- [10] J. Du, K. Hu, J. Zhang, L. Meng, J. Yue, I. Angunawela, H. Yan, S. Qin, X. Kong, Z. Zhang, B. Guan, H. Ade, Y. Li, A molecular photosensitizer achieves a Voc of 1.24 V enabling highly efficient and stable dye-sensitized solar cells with copper (II/I)-based electrolyte, *Nat. Commun.* 12 (1) (2021) 1–10.
- [11] F. Du, X. Zuo, Q. Yang, G. Li, Z. Ding, M. Wu, Y. Ma, K. Zhu, Nanohybrids of RGO nanosheets and 2-dimensional porous Co₃O₄ nanoflakes working as highly efficient counter electrodes for dye-sensitized solar cells, *J. Mater. Chem. C* 4 (2016) 10323–10328, <https://doi.org/10.1039/c6tc03540j>.
- [12] F. Gong, H. Wang, X. Xu, G. Zhou, Z.S. Wang, In situ growth of Co_{0.85}Se and Ni_{0.85}Se on conductive substrates as high-performance counter electrodes for dye-sensitized solar cells, *J. Am. Chem. Soc.* 134 (2012) 10953–10958, <https://doi.org/10.1021/ja303034w>.
- [13] M. Guo, B. Tang, H. Zhang, S. Yin, W. Jiang, Y. Zhang, M. Li, H. Wang, L. Jiao, A high efficiency CoCr₂O₄/carbon nanotubes nanocomposite electrocatalyst for dye-sensitized solar cells, *Chem. Commun.* 50 (2014) 7356–7358, <https://doi.org/10.1039/c4cc03221g>.
- [14] L. Kavan, H. Kryssova, P. Janda, H. Tarabkova, Y. Saygili, M. Freitag, S. M. Zakeeruddin, A. Hagfeldt, M. Grätzel, Novel highly active Pt/graphene catalyst for CEs of Cu(II/I)-mediated dye-sensitized solar cells, *Electrochim. Acta* 251 (2017) 167–175, <https://doi.org/10.1016/j.electacta.2017.08.080>.
- [15] Y. Kim, K. Bicanic, H. Tan, O. Ouellette, B.R. Sutherland, F.P. Garcia de Arquer, J. W. Jo, M. Liu, B. Sun, M. Liu, S. Hoogland, E.H. Sargent, Nanoimprint-transfer-patterned solids enhance light absorption in colloidal quantum dot solar cells, *Nano Lett.* 17 (2017) 2349–2353, <https://doi.org/10.1021/acs.nanolett.6b05241>.
- [16] S. Xu, N. Cheng, H. Yin, D. Cao, B. Mi, Electrospay preparation of CuInS₂ films as efficient counter electrode for dye-sensitized solar cells (Article), *Chem. Eng. J.* 397 (2020), 125463, <https://doi.org/10.1016/j.cej.2020.125463>.
- [17] P. Xie, Y. Yao, Z. Huang, Z. Liu, J. Zhang, T. Li, G. Wang, R. Shahbazian-Yassar, L. Hu, C. Wang, Highly efficient decomposition of ammonia using high-entropy alloy catalysts, *Nat. Commun.* 10 (2019) 1–12, <https://doi.org/10.1038/s41467-019-11848-9>.
- [18] M.T. Greiner, T.E. Jones, S. Beeg, L. Zwiener, M. Scherzer, F. Girsig, S. Piccinin, M. Armbrüster, A. Knop-Gericke, R. Schlögl, Free-atom-like d states in single-atom alloy catalysts, *Nat. Chem.* 10 (2018) 1008–1015, <https://doi.org/10.1038/s41557-018-0125-5>.
- [19] J. Yao, W. Wang, X. Zuo, Q. Yang, M.W. Khan, M. Wu, H. Tang, S. Jin, G. Li, Multi-interface superstructure strategy to improve the catalytic activity and cyclic stability in enhancing the photo conversion in solar cells (Article), *Appl. Catal. B: Environ.* 256 (2019), 117857, <https://doi.org/10.1016/j.apcatb.2019.117857>.
- [20] S.P. Borderud, Y. Li, J.E. Burkhalter, C.E. Sheffer, J.S. Ostroff, Electronic cigarette use among patients with cancer: characteristics of electronic cigarette users and their smoking cessation outcomes, *Cancer* 121 (2015), 800, <https://doi.org/10.1002/adfm.201803973>.
- [21] M. Arivu, J. Masud, S. Umapathi, M. Nath, Facile synthesis of Ni₃B/rGO nanocomposite as an efficient electrocatalyst for the oxygen evolution reaction in alkaline media, *Electrochem. Commun.* 86 (2018) 121–125, <https://doi.org/10.1016/j.elecom.2017.12.002>.
- [22] K. Han, Z. Liu, P. Li, Q. Yu, W. Wang, C.-Y. Lao, D. He, W. Zhao, G. Suo, H. Guo, L. Song, M. Qin, X. Qu, High-throughput fabrication of 3D N-doped graphenic framework coupled with Fe₃C@porous graphite carbon for ultrastable potassium ion storage, *Energy Storage Mater.* 22 (2019) 185–193, <https://doi.org/10.1016/j.ensm.2019.01.016>.
- [23] S.P. Borderud, Y. Li, J. E Burkhalter, C.E. Sheffer, J.S. Ostroff, J. Chen, Electronic cigarette use among patients with cancer: Characteristics of electronic cigarette users and their smoking cessation outcomes, *Cancer* 121 (2015), 800, <https://doi.org/10.1002/aenm.201400337>.
- [24] J. Yao, K. Zhang, W. Wang, X. Zuo, Q. Yang, H. Tang, M. Wu, G. Li, Remarkable enhancement in the photoelectric performance of uniform flower-like mesoporous Fe₃O₄ wrapped in nitrogen-doped graphene networks, *ACS Appl. Mater. Interfaces* 10 (2018) 19564–19572, <https://doi.org/10.1021/acsami.8b01240>.
- [25] Z. Xu, Y. Du, D. Liu, Y. Wang, W. Ma, Y. Wang, P. Xu, X. Han, Pea-like Fe/Fe₃C nanoparticles embedded in nitrogen-doped carbon nanotubes with tunable dielectric/magnetic loss and efficient electromagnetic absorption, *ACS Appl. Mater. Interfaces* 11 (2019) 4268–4277, <https://doi.org/10.1021/acsami.8b19201>.
- [26] X. Sun, P. Wei, S. Gu, J. Zhang, Z. Jiang, J. Wan, Z. Chen, L. Huang, Y. Xu, C. Fang, Q. Li, J. Han, Y. Huang, Atomic-level Fe–N–C coupled with Fe₃C–Fe nanocomposites in carbon matrices as high-efficiency bifunctional oxygen catalysts, *Small* 16 (2020), 1906057, <https://doi.org/10.1002/sml.201906057>.
- [27] Z. Yang, Y. Wang, M. Zhu, Z. Li, W. Chen, W. Wei, T. Yuan, Y. Qu, Q. Xu, C. Zhao, X. Wang, P. Li, Y. Li, Y. Wu, Y. Li, Boosting oxygen reduction catalysis with Fe–N₄ sites decorated porous carbons toward fuel cells, *ACS Catal.* 9 (2019) 2158–2163, <https://doi.org/10.1021/acscatal.8b04381>.
- [28] N. Cheng, S. Stambula, D. Wang, M.N. Banis, J. Liu, A. Riese, B. Xiao, R. Li, T. K. Sham, L.M. Liu, G.A. Botton, X. Sun, Platinum single-atom and cluster catalysis of the hydrogen evolution reaction, *Nat. Commun.* 7 (2016), 13638, <https://doi.org/10.1038/ncomms13638>.
- [29] Z. Wen, S. Ci, F. Zhang, X. Feng, S. Cui, S. Mao, S. Luo, Z. He, J. Chen, Nitrogen-enriched core-shell structured Fe/Fe₃C–C nanorods as advanced electrocatalysts for oxygen reduction reaction, *Adv. Mater.* 24 (2012) 1399–1404, <https://doi.org/10.1002/adma.201104392>.
- [30] X. Xin, H. Qin, H.-P. Cong, S.-H. Yu, Templating synthesis of mesoporous Fe₃C-encapsulated Fe–N-doped carbon hollow nanospindles for electrocatalysis, *Langmuir* 34 (2018) 4952–4961, <https://doi.org/10.1021/acs.langmuir.8b00548>.
- [31] X. Li, Y. Zhang, S. Wang, Y. Liu, Y. Ding, G. He, N. Zhang, G. Yu, Hierarchically porous C/Fe₃C membranes with fast ion-transporting channels and polysulfide-trapping networks for high-areal-capacity Li–S batteries, *Nano Lett.* 20 (2020) 701–708, <https://doi.org/10.1021/acs.nanolett.9b04551>.
- [32] W.J. Jiang, L. Gu, L. Li, Y. Zhang, X. Zhang, L.J. Zhang, J.Q. Wang, J.S. Hu, Z. Wei, L.J. Wan, Understanding the high activity of Fe–N–C electrocatalysts in oxygen reduction: Fe/Fe₃C nanoparticles boost the activity of Fe–N_(x), *J. Am. Chem. Soc.* 138 (2016) 3570–3578, <https://doi.org/10.1021/jacs.6b00757>.
- [33] S.P. Borderud, J.E. Burkhalter, C.E. Sheffer, J.S. Ostroff, Electronic cigarette use among patients with cancer: characteristics of electronic cigarette users and their smoking cessation outcomes, *Cancer* 121 (2015), 800, <https://doi.org/10.1002/adfm.201901531>.
- [34] X. Meng, C. Yu, X. Song, J. Iocozzia, J. Hong, M. Rager, H. Jin, S. Wang, L. Huang, J. Qiu, Z. Lin, Scrutinizing defects and defect density of selenium-doped graphene for high-efficiency triiodide reduction in dye-sensitized solar cells, *Angew. Chem. Int. Ed.* 57 (2018) 4682–4686, <https://doi.org/10.1002/anie.201801337>.
- [35] A. Sarkar, A.K. Chakraborty, S. Bera, NiS/rGO nanohybrid: an excellent counter electrode for dye sensitized solar cell, *Sol. Energy Mater. Sol. Cells* 182 (2018) 314–320, <https://doi.org/10.1016/j.solmat.2018.03.026>.
- [36] S.P. Borderud, Y. Li, J.E. Burkhalter, C.E. Sheffer, J.S. Ostroff, Electronic cigarette use among patients with cancer: characteristics of electronic cigarette users and their smoking cessation outcomes, *Cancer* 121 (2015), 800, <https://doi.org/10.1002/aenm.201602276>.
- [37] W. Wang, J. Yao, X. Zuo, Q. Yang, M. Wu, H. Tang, S. Jin, G. Li, Multifunctional hollow sandwich structure with many active sites for electronic transfer

- modulation and its application in energy storage and conversion, *Nanoscale Horiz.* 4 (2019) 1211–1220, <https://doi.org/10.1039/c9nh00133f>.
- [38] J. Hu, A.G. Kontos, C.A. Georgiou, M. Bidikoudi, N. Stein, B. Breen, P. Falaras, Combining dc and ac electrochemical characterization with micro Raman analysis on industrial DSCs under accelerated thermal stress, *Electrochim. Acta* 271 (2018) 268–275, <https://doi.org/10.1016/j.electacta.2018.03.125>.
- [39] W. Yang, X. Xu, Y. Gao, Z. Li, C. Li, W. Wang, Y. Chen, G. Ning, L. Zhang, F. Yang, S. Chen, A. Wang, J. Kong, Y. Li, High-surface-area nanomesh graphene with enriched edge sites as efficient metal-free CE for dye-sensitized solar cells, *Nanoscale* 8 (2016) 13059–13066, <https://doi.org/10.1039/c6nr01838f>.
- [40] J. Yao, K. Zhang, W. Wang, X. Zuo, Q. Yang, H. Tang, M. Wu, G. Li, Functional integration and self-template synthesis of hollow core-shell carbon mesoporous spheres/Fe₃O₄/nitrogen-doped graphene to enhance catalytic activity in DSSCs, *Nanoscale* 10 (2018) 7946–7956, <https://doi.org/10.1039/c8nr01095a>.
- [41] C. Yu, X. Meng, X. Song, S. Liang, Q. Dong, G. Wang, C. Hao, X. Yang, T. Ma, P. M. Ajayan, J. Qiu, Graphene-mediated highly-dispersed MoS₂ nanosheets with enhanced triiodide reduction activity for dye-sensitized solar cells, *Carbon* 100 (2016) 474–483, <https://doi.org/10.1016/j.carbon.2016.01.042>.
- [42] F. Yu, Y. Shi, X. Shen, W. Yao, S. Han, J. Ma, Three-dimensional MoS₂-nanosheet-based graphene/carbon nanotube aerogel as a Pt-free counter electrode for high-efficiency dye-sensitized solar cells, *ACS Sustain. Chem. Eng.* 6 (2018) 17427–17434, <https://doi.org/10.1021/acssuschemeng.8b03143>.
- [43] Z. Zhao, C.-Y. Lin, J. Tang, Z. Xia, Catalytic mechanism and design principles for heteroatom-doped graphene catalysts in dye-sensitized solar cells, *Nano Energy* 49 (2018) 193–199, <https://doi.org/10.1016/j.nanoen.2018.04.053>.
- [44] M. Chen, G.C. Wang, L.L. Shao, Z.Y. Yuan, X. Qian, Q.S. Jing, Z.Y. Huang, D.L. Xu, S.X. Yang, Strategic design of vacancy-enriched Fe_{1-x}S nanoparticles anchored on Fe₃C-encapsulated and N-doped carbon nanotube hybrids for high-efficiency triiodide reduction in dye-sensitized solar cells, *ACS Appl. Mater. Interfaces* 10 (2018) 31208–31224, <https://doi.org/10.1021/acsami.8b08489>.
- [45] J. Yao, K. Zhang, W. Wang, X. Zuo, Q. Yang, M. Wu, G. Li, Great enhancement of electrochemical cyclic voltammetry stabilization of Fe₃O₄ microspheres by introducing 3DRGO, *Electrochim. Acta* 279 (2018) 168–176, <https://doi.org/10.1016/j.electacta.2018.05.088>.
- [46] B. Yang, X. Zuo, P. Chen, L. Zhou, X. Yang, H. Zhang, G. Li, M. Wu, Y. Ma, S. Jin, X. Chen, Nanocomposite of tin sulfide nanoparticles with reduced graphene oxide in high-efficiency dye-sensitized solar cells, *ACS Appl. Mater. Interfaces* 7 (2015) 137–143, <https://doi.org/10.1021/am5040522>.
- [47] E. Bi, H. Chen, X. Yang, W. Peng, M. Grätzel, L. Han, A quasi core-shell nitrogen-doped graphene/cobalt sulfide conductive catalyst for highly efficient dye-sensitized solar cells, *Energy Environ. Sci.* 7 (2014) 2637–2641, <https://doi.org/10.1039/c4ee01339e>.
- [48] S. Liang, C. Zhu, N. Zhang, S. Zhang, B. Qiao, H. Liu, X. Liu, Z. Liu, X. Song, H. Zhang, C. Hao, Y. Shi, A novel single-atom electrocatalyst Ti₁/rGO for efficient cathodic reduction in hybrid photovoltaics, *Adv. Mater.* 32 (2020), 2000478, <https://doi.org/10.1002/adma.202000478>.
- [49] Y. Chen, Z. Li, Y. Zhu, D. Sun, X. Liu, L. Xu, Y. Tang, Atomic Fe dispersed on N-doped carbon hollow nanospheres for high-efficiency electrocatalytic oxygen reduction (Article), *Adv. Mater.* 31 (2019), 1806312, <https://doi.org/10.1002/adma.201806312>.
- [50] K. Yuan, S. Sfaelou, M. Qiu, D. Lützenkirchen-Hecht, X. Zhuang, Y. Chen, C. Yuan, X. Feng, U. Scherf, Synergetic contribution of boron and Fe-N_x species in porous carbons toward efficient electrocatalysts for oxygen reduction reaction, *ACS Energy Lett.* 3 (2017) 252–260, <https://doi.org/10.1021/acsenenergylett.7b01188>.